ENGINEERING

Self-supervised AI for decoding and designing disordered metamaterials

Min Shen[1], Ke Liu[2]*, Sheng Mao[1]*, Chiara Daraio[3]

Disordered microstructures are key to the distinct multifunctional properties of many natural materials. However, understanding the relationship between their microstructures and physical functions remains formidable, hindering engineering applications. Here, we introduce a physics-guided, self-supervised artificial intelligence (AI) framework called generative networks for disordered metamaterials (GNDM), trained on a progressively expanding dataset starting from a few initial samples. We integrate a formula writing module in the training process of neural networks to enforce the identification of the most selective set of hidden geometric invariants that dictate bulk properties. By inversely solving the formulae, GNDM manipulate disordered geometric features to extrapolate property space and design previously unknown structures via its generator module, validated by experiments. GNDM offers an all-in-one AI framework that closes the loop of feature extraction, property prediction, formula writing, and inverse design, unraveling the regulative role of disorder, a critical challenge in the study of metamaterials with complex microstructures.

INTRODUCTION

Natural materials—such as wood (*1*), sea sponge ridges (*2*), turtle shells (*3*), coral (*4*) (Fig. 1A), and human bones (*5*)—often feature complex microstructures (*6*), characterized by their disorderedness, nonuniformity, and aperiodicity. These microstructures are the result of evolutionary processes to achieve certain optimal functions, such as body support (*7*), tissue remodeling, and stress shielding. In engineering, fueled by the ability to fabricate fine structures with the advent of additive manufacturing, metamaterials are created to exploit complex microstructures for unusual properties (*8*–*11*). However, their microstructures are mostly ordered and periodic, as reported in electromagnetics (*12*, *13*), acoustics (*14*, *15*), batteries (*16*), and robotics (*17*, *18*). This is in stark contrast to many biologically derived materials observed in nature, which are both functionally efficient and structurally disordered. These observations suggest that incorporating randomness into the design of metamaterials could offer yet-unexplored advantages. For instance, structural irregularities can increase a material's resilience to defects, allowing it to mitigate strong stress concentrations or symmetry-breaking failures (*19*, *20*). Moreover, these irregularities can lead to unique mechanical properties, including unconventional stiffness-to-weight scaling (*21*), increased failure resistance (*9*, *10*), stress modulation (*22*), and tunable negative Poisson's ratios (*23*). However, the investigation of disordered materials remains in its nascent stage, with limited studies aiming to understand their structure-property relationships and design principles (*24*–*26*). This is because conventional descriptors of geometries cannot effectively describe disordered microstructures in a meaningful way (*27*). These challenges underline the importance of developing models that define geometric characteristics of disordered microstructures and connect them with bulk material properties.

The rapid development of artificial intelligence (AI) offers a great opportunity to address this challenge (*28*–*33*). Disordered microstructures can be essentially described by certain high-dimensional probability distributions (*34*, *35*) and AI models, particularly deep generative models that are well known for their efficiency in approximating complex, high-dimensional distributions. For example, generative adversarial networks (GANs) have been used to decrease the computational cost of topology optimization on large datasets (*36*, *37*), while variational autoencodes have been used for structure reconstruction (*38*). Here, we propose a physics-guided, self-supervised, scalable framework, which we call generative networks for disordered metamaterial (GNDM, pronounced as "Gundam"), to learn property-structure relationships and design new disordered metamaterials with desired properties. GNDM relies only on an unlabeled training set of data representing material microstructures and physical simulation tools, without the need for convoluted pre- and postprocessing. The framework models microstructures as a collection of small voxels, with each voxel representing one type of constituent material. Because we are dealing with nondeterministic, disordered microstructures, we assume that these microstructures can be generated by drawing random samples from a probability distribution characterized by a set of parameters $\{\boldsymbol{\alpha}^{M}\}$. These parameters shall characterize the geometric features of arbitrary-disordered microstructures. The corresponding material properties are also random variables whose probability distribution is governed by parameters $\{\boldsymbol{\alpha}^{P}\}$. The core of this work is to use a series of neural networks (*39*–*41*) in conjunction with a formula writing module to establish a direct, reliable, and interpretable connection between $\{\boldsymbol{\alpha}^{M}\}$ and $\{\boldsymbol{\alpha}^{P}\}$ (Fig. 1A). Understanding this relationship between structures and properties offers a framework for efficient structural design of new materials.

Unlike traditional methods that use deterministic description for both structures and properties, our approach is better suited for disordered microstructures by treating both as random variables governed by distribution parameters. This probabilistic framework enables direct modeling of uncertainty and captures the intrinsic variability of disordered structures. Based on this framework, the hidden structure-property relationship is uncovered through the direct connection between $\{\boldsymbol{\alpha}^{M}\}$ and $\{\boldsymbol{\alpha}^{P}\}$ by the formula writing

[1]Department of Mechanics and Engineering Science, College of Engineering, Peking University, Beijing 100871, PR China. [2]Department of Advanced Manufacturing and Robotics, College of Engineering, Peking University, Beijing 100871, PR China. [3]Division of Engineering and Applied Science, California Institute of Technology, Pasadena, California 91125, USA.
*Corresponding author. Email: liuke@pku.edu.cn (K.L.); maosheng@pku.edu.cn (S.M.)

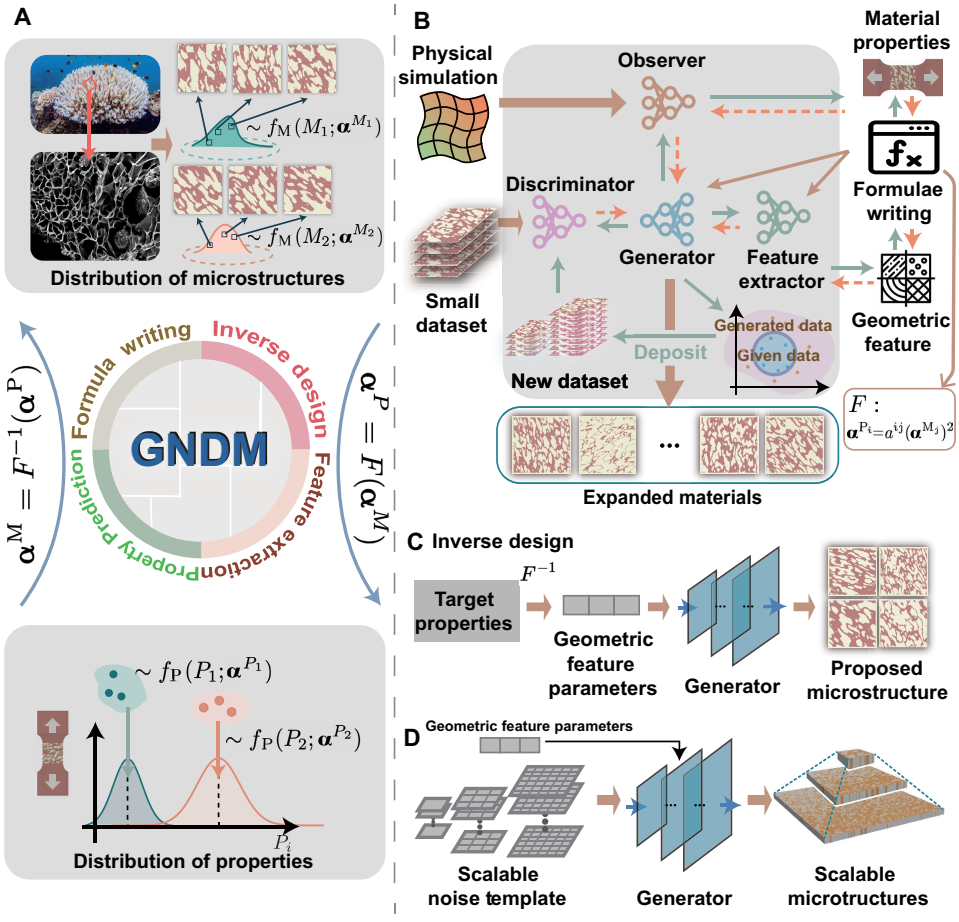

Fig. 1. Overview of the GNDM. (**A**) Heterogeneous and disordered microstructures of coral fibers, which result from incremental growth during biomineralization (*4*). The distributions of these microstructures' geometric features f_M can be characterized by the parameter $\{\boldsymbol{\alpha}^M\}$, while the distributions of properties f_P arising from these microstructures can be described by the parameter $\{\boldsymbol{\alpha}^P\}$. The relationship between these two distributions is unveiled by GNDM. (**B**) Schematic of the workflow. GNDM takes a set of base materials and a physical simulation algorithm as input and outputs the microstructure with desired properties by learning the relationship between geometric features and properties. (**C**) Inverse design process with target properties. The input geometric feature parameters are obtained by solving phenomenological formula. Then, these parameters are fed into the generator, which produces a structure that meets the specified requirements. (**D**) GNDM generates coherent designs that occupy arbitrary space regardless of the geometric size of the training samples.

module, which provides feedback to the feature extractor network to accurately identify the key geometric features out of many possibilities that dictate mechanical properties. Furthermore, targeting at material property $\{\boldsymbol{\alpha}^P\}$, we can inversely calculate the associated $\{\boldsymbol{\alpha}^M\}$ to sample new designs that are both creative and consistent with the learned distribution.

For instance, we demonstrate that we can effectively expand the range of material properties within the dataset by more than 60%, including Young's modulus, surface area, and the direction of maximum stiffness. By depositing these designs in an expanded dataset, we can retrain the model to preserve its performance across this broader spectrum of properties.

RESULTS

GNDM'S architecture

The GNDM consists of four neural network modules, physical simulation tools, and a (phenomenological) formula writing module (Fig. 2A). The physical simulation tools are responsible for computing material properties based on microstructures, which include several image-based algorithms, such as calculating the effective Young's modulus by finite element method (FEM) and the relative surface area by marching cube algorithms.

The four neural network modules include a generator, a discriminator, a feature extractor, and an observer. The generator network produces designs of material microstructures and eventually serves as the tool for designing materials with desired properties (Fig. 1, C and D). The discriminator measures the similarity of the training material samples and the generated material samples. For detailed architectures of the generator and discriminator, see fig. S1. The feature extractor is responsible for extracting the parameters $\{\boldsymbol{\alpha}^M\}$ from the generated microstructures, which describe the probability distribution of the geometric features of material microstructures. The observer targets another set of parameters $\{\boldsymbol{\alpha}^P\}$, which describes the probability distribution of material properties. In practice, we have found that simply treating the $\{\boldsymbol{\alpha}^P\}$ as the mean of the material properties' distribution $\overline{\mathbf{P}}$ is sufficient for characterizing their probability distributions. The observer is a differentiable surrogate model of the

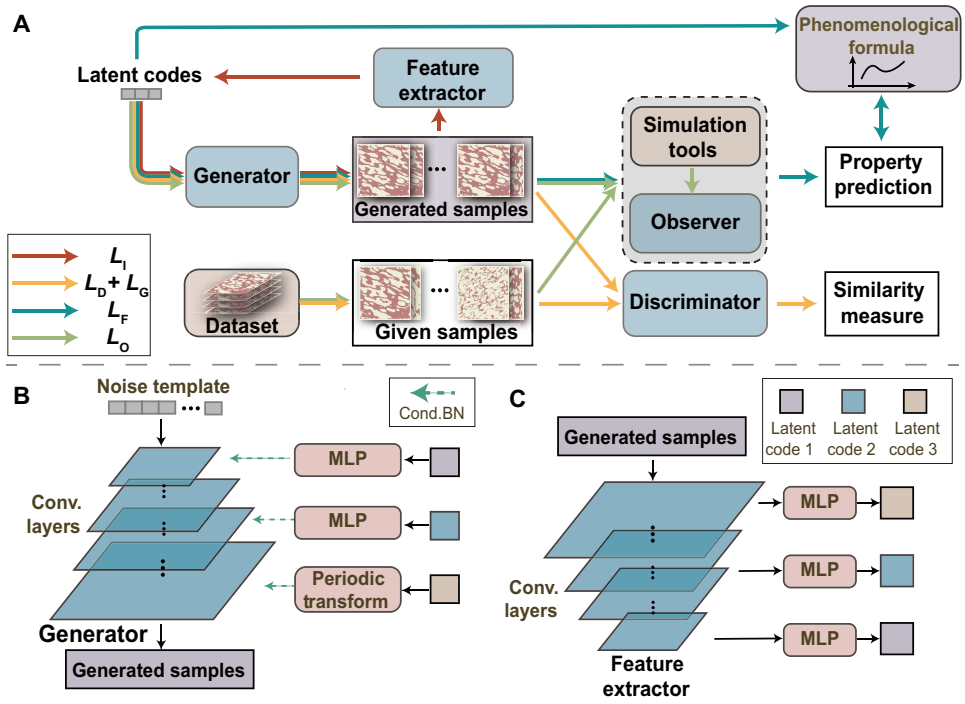

Fig. 2. Detailed network architectures of the GNDM. (**A**) Illustration of the workflow of GNDM. The flow of information for calculating different losses is represented by different colored arrows. The red arrows represent the workflow for maximizing mutual information to extract a parameterization of relevant geometric features for expected material properties. The yellow arrows represent the classic WGAN-GP (*40*) workflow, optimizing the generator and discriminator to generate realistic samples. The bottle green arrows demonstrate the fitting-loss workflow, aiming to establish the relationship between material properties and extract principal geometric features that determine bulk material properties. The pale green arrows illustrate the optimization workflow for the observer. (**B**) Latent code input mechanism in the generator for a three-parameter case. The input latent code is fed into the network from various layers using conditional batch normalization, implemented either via a fully connected layer or periodic transformation (in the case of periodic latent code). BN, batch normalization; MLP, multilayer perceptron. (**C**) Latent code information output mechanism in the feature extractor for a three-parameter case. Combined with the position of the latent code input layer, the latent code information is restored through the fully connected layers, which followed by the corresponding layers of the CNN network.

physical simulation tools, which is responsible for providing the generator with the gradient information from the probability distribution of material properties—it can also be used to accelerate the calculation of material properties. The formula writing module aims to summarize the relationship between the $\{\boldsymbol{\alpha}^{M}\}$ and $\{\boldsymbol{\alpha}^{P}\}$ by establishing an interpretable mapping between the probability distributions of disordered geometries and material properties. This is implemented by relating $\{\boldsymbol{\alpha}^{M}\}$ and $\{\boldsymbol{\alpha}^{P}\}$ by some closed-form, phenomenological equations. The fitting error (L_F) is then fed back to the neural networks to force the feature extractor to identify geometric features that are more relevant to the concerned properties.

To capture the geometric features of materials in the dataset, we decompose the input of the generator into two parts, the incompressible input noise templates, and the latent codes $\mathbf{c}$ that aim at representing the parameters α^{M}. By maximizing the mutual information between latent codes $\mathbf{c}$ and the generator's distribution (*41*), the framework extracts disentangled geometric representations in a physics-guided, self-supervised manner. To do so, we use the feature extractor to approximate the true posterior probability of the latent codes $\mathbf{c}$. Consequently, the latent codes $\mathbf{c}$, serving as specialized geometric parameters, determine the material geometric features. The input noise templates consist of multidimensional random values, introducing stochastic variations into the final disordered microstructural designs.

The main objective of the GNDM is to automatically learn the structure-property relationship of disordered microstructures from a small dataset and design material microstructures for an expanded property space. The generated materials are then fed into the discriminator, the observer, and the feature extractor, each providing feedback to the generator. This feedback loop allows the generator to follow the similarity constraint, the disentangled representation constraint, and the physical constraint, all at once. It is vital to fine-tune the extra hyperparameters of the constraint coefficients to balance GNDM's performance trade-off, enabling the generator to produce desired materials while maintaining the efficiency of latent codes and accuracy of the phenomenological formula.

The total loss L for training is defined as $L = \lambda_G L_G + \lambda_D L_D + \lambda_I L_I + \lambda_O L_O + \lambda_F L_F$, where each λ_i denotes the weight assigned to different loss components. L_G and L_D denote the losses of the generator and discriminator in Wasserstein GAN with gradient penalty (WGAN-GP) (*40*), respectively. The loss L_I represents the variational lower bound of the mutual information between a small subset of the latent variables and the observation. The loss L_O represents the mean square error (MSE) loss for optimizing the observer, and L_F represents the MSE loss of the predicted properties obtained from the observer and that from the phenomenological formula (for additional details on the loss function, refer to Materials and Methods). To provide the generator with precise gradients on the target properties, encompassing

both the training microstructures and the generated ones, the GNDM relies on a closed-loop that integrates the simulation tools into the pipeline, rather than using a pretrained network to obtain material properties. Note that in our framework, simulation tools are integrated into the pipeline to provide internal supervision signals, rather than external human-annotated labels.

For better convergence, we use a multistage optimization process to train the GNDM. In the first stage, we only optimize the generator network, the discriminator network, and the observer. The corresponding loss is $L_1 = \lambda_G L_G + \lambda_D L_D + \lambda_O L_O$. This stage focuses on the basic generative capability of the generator and the prediction capability of the observer. In the following stage, we incorporate the training of the feature extractor network, and the loss function is then updated as $L_2 = L_1 + \lambda_I L_I$. This encourages the framework to acquire an interpretable representation of the structure-property relationship. Last, in the main stage, we optimize the phenomenological formula based on the loss function L using fixed point methods. Because we extract the interpretable geometric features in stage 2, the optimization of the coefficients of the phenomenological formula has a better convergence than directly putting together all of the loss.

Establishing interpretable structure-property relationship

The spatial characteristics of the disordered structures are determined by the parameters $\{\boldsymbol{\alpha}^M\}$. Note that $\{\boldsymbol{\alpha}^M\}$ does not determine the geometry of particular microstructures; instead, it characterizes the probability distribution that generates the disordered microstructures. In other words, each microstructural design of the disordered metamaterial is regarded as a sample drawn from the probability distribution defined by $\{\boldsymbol{\alpha}^M\}$. To achieve better disentanglement and interpretability with multiscale information, we extract geometric features at different levels with the help of convolutional neural networks (CNNs), which are well-known for capturing information at various scales, with deeper layers capable of extracting more intricate details. The corresponding material properties of a particular microstructure can be computed by the physical simulation tool. Rather than focusing on the deterministic values of a particular microstructure, we also treat the material properties in a statistical sense. Although the final generated materials have different spatial arrangements for the same input geometric parameters $\{\boldsymbol{\alpha}^M\}$, their properties follow the probability distribution defined by material property parameters $\{\boldsymbol{\alpha}^P\}$.

To establish a predictive and interpretable connection between geometric features and material properties, we seek to characterize the relationship between $\{\boldsymbol{\alpha}^M\}$ and $\{\boldsymbol{\alpha}^P\}$ in closed-form equations by incorporating the formula writing module. We approximate this complex relationship by a phenomenological formula projected as polynomials with a finite number of terms. The magnitude of each coefficient essentially explains how important the geometric feature is to the corresponding material property. The optimization process for both the generator and the phenomenological formula follows a fixed-point algorithm, where we iteratively optimize the generator using the phenomenological formula and refine the phenomenological formula based on the properties of the generated materials. This approach serves for three main purposes: First, the phenomenological formula elucidates the connection between the distribution of geometry and material properties and presents it in an interpretable way and thus uncovers the regulative role of disorder in dictating material properties. In the optimized phenomenological formula representation, the polynomial coefficients are the bridge between the distribution of material properties and the distribution of geometric features. Each coefficient quantifies how strongly a latent code contributes to the physical property. Accordingly, larger absolute values indicate stronger correlation between the material property to the corresponding geometric feature, while smaller absolute values indicate weaker influence. Second, the loss term L_F can be seen as a physics-informed constraint on the generator that helps to identify the set of geometric features that are most relevant to the target properties. Last but not least, by inversely solving this formula, the generator can be guided to manipulate the disordered microstructures to achieve target properties. This feature is vital to expand the material property space and to inverse design, which we shall discuss in the following text.

Expanding the material property space via iterative deposit-retrain in an automatic manner

Continuous variation of material microstructures will result in continuous variation of material properties. In GNDM, this will be reflected by a gradual change in the latent code. By designing materials that extrapolate new geometric features, we obtain materials with expanded material properties through creative combinations of spatial patterns. By leveraging the advantage of disentangled and interpretable geometric feature variations, we can interpolate and extrapolate the geometric features to design materials with relevant properties in an expanded, continuous property space. This is achieved by interpolating and extrapolating the learned parameters of the probability distributions of the geometric features, i.e., the latent codes, and by retraining the network with the new dataset enriched by the newly generated microstructures with out-of-domain properties.

As the discriminator is learned from the initial dataset, it lacks the capability to discern the data generated by the extrapolated latent codes. To address this issue, we propose a previously unidentified deposit-retrain method (Fig. 1B) to expand the design space. First, we generate new materials by extrapolating the latent codes. Then, the material properties of these generated materials are calculated via the physical simulation tools. If the material properties are outside the property space of the previous dataset, they are deposited into a new, expanded dataset. Last, we retrain the networks on the new datasets while keeping the phenomenological formula fixed. The input latent codes of the generator are reconfigured to recognize the new geometric features of the generated materials. This process allows us to generate materials that reasonably follow the learned phenomenological formula. The retraining procedure substantially enhanced the preservation of the learned relationship between the probability distribution of the geometric features and the material properties, as evidenced in Fig. 3C. Using this approach, we can efficiently explore the entire design space of disordered structures with physical constraints, offering means to explore the disordered metamaterial designs comprehensively and systematically.

Generating disordered microstructures

Now that we have established the relationship between probability distributions of geometric features and material properties, we proceed to construct an efficient design process (Fig. 1C). As a first step, we inversely solve the phenomenological formula to obtain the input latent codes $\mathbf{c}$ that meet the target mean properties. Then, the latent codes are fed to the generator to yield the desired microstructures. Our approach is scale-free, i.e., it can be used for the design of

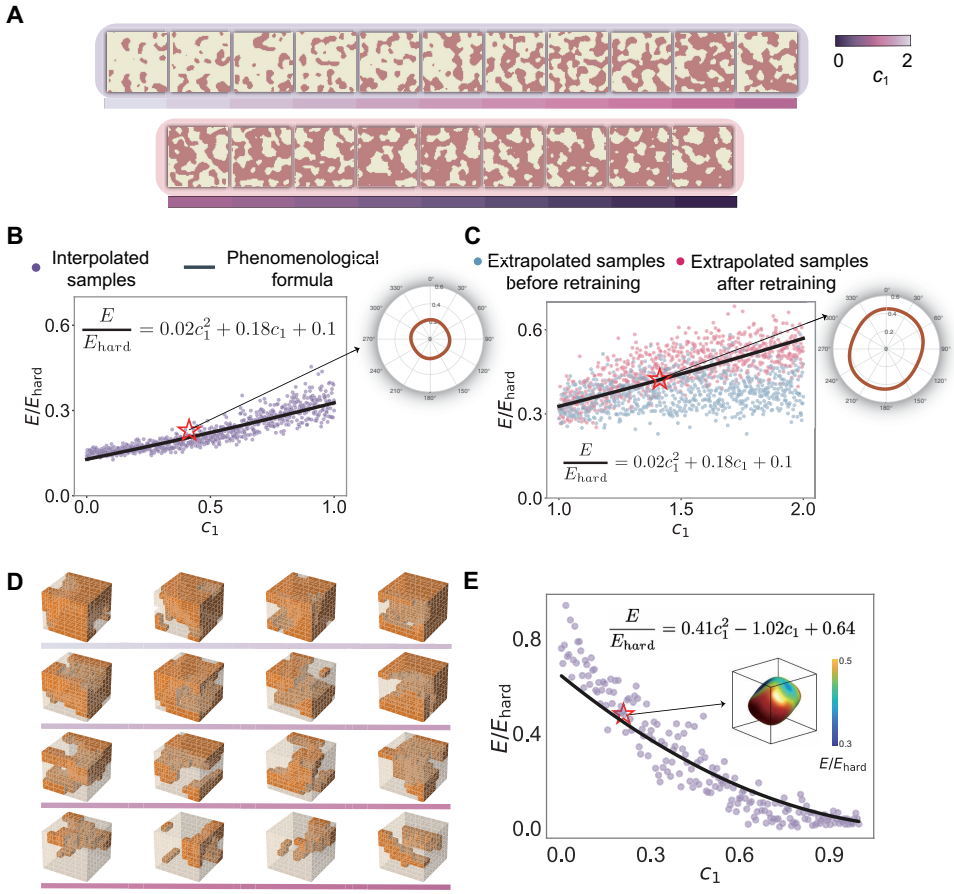

Fig. 3. Examples in 2D and 3D for a single pair of materialproperty and geometric feature. (**A**) Generated 2D samples with random noise templates and gradual changes in latent codes. (**B**) Comparison between the Young's moduli (normalized by E_{hard}, the Young's modulus of the hard material) predicted by the phenomenological formula and FEM for generated interpolated samples within the range of the given dataset. This includes results of the directional Young's modulus at a typical point. (**C**) Comparison between the elastic moduli predicted by the phenomenological formula and FEM for the generated extrapolated samples before and after retraining outside the range of the given dataset, including results of the directional Young's modulus at a typical point. (**D**) 3D generated materials with gradual modifications in latent codes. (**E**) Comparison between the elastic moduli predicted by the phenomenological formula and FEM, including the directional Young's modulus at a selected point.

spatially varying materials with arbitrary sizes, without the need to address interface matching issues between regions with different local properties (*42*, *43*). As demonstrated in Fig. 1D, to produce structures with different sizes, we can simply alter the size of the corresponding input noise template and the latent code. These structures can be seen as a mosaic composed of numerous generated microstructures, each of which shares the same geometric size as the ones in the dataset and is generated using the same generator parameters. In the generator, the upsampling interpolation ensures coherent local structures. In addition, by fine-tuning the local input latent codes, this approach can also be applied to generate functionally graded materials (figs. S8 to S10). Such an approach holds great potential for hierarchical design (*44*–*46*) and the engineering of functionally graded materials (*34*, *47*).

GNDM'S performance on disordered two-phase metamaterials

To validate the effectiveness of GNDM, we conduct tests on a dataset of two-dimensional (2D) disordered metamaterials with varying volume fractions. We adopt a random-field description of the materials, with the interface between the phases defined by contours of Gaussian random field (GRF) (*27*, *34*). For details, see Materials and Methods.

We define a single geometric parameter c_1 (i.e., the latent code) to describe the probability distribution of geometric features. Our objective is to design materials with target Young's modulus. The simulation tools include FEM to calculate the effective Young's modulus for a given piece of input material. This geometric parameter turns out to be strongly associated with the relative fraction of the two material phases, which is consistent with what has been found in the literature (*48*).

The results of our numerical experiments are shown in Fig. 3 (A to C). By changing the latent code c_1, apparent variations in the spatial patterns of the material microstructures can be observed, directly associated with the relative fraction of the two materials. The automatically found latent code plays a pivotal role in determining the mean Young's modulus of the generated materials. In Fig. 3 (A and C), we also present the generated materials in the extrapolated property space. These materials inherit the probability distribution of the geometric feature learned from the initial dataset yet exhibit material

properties that fall outside the range of the dataset. After retraining, we ensure that the mean Young's modulus relates to the extrapolated latent code following the optimized phenomenological formula.

To further illustrate the GNDM's workflow in disentangling multiple disordered geometric features, we conduct tests on an enriched dataset of materials with skewed microstructures and anisotropic properties. Our objective is to design materials with multiple target properties, including stiffness (i.e., Young's modulus), porosity (i.e., relative surface area), and anisotropy (i.e., the direction of maximum stiffness). These three critical physical properties have broad applications in a variety of fields. For instance, they play a crucial role in aerospace engineering, geoscience, and biological engineering (*30*, *49*).

For these multifunctional designs, we keep two of the three latent codes c_1 to c_3 constant and only change one of them. The results in Fig. 4 (A to C) show the variations of microstructures when c_1, c_2, and c_3 are chosen as the varying latent codes, respectively. According to our observations, the geometric features associated with c_1 are related to the relative proportion of the two constituent materials, those of c_2 determine the interfacial area, and those of c_3 capture the features related to the anisotropy of the materials. The probability distributions for each pair of properties are shown in fig. S2. To more demonstrate the specific geometric feature of the microstructure that controlled by c_1, c_2, and c_3, Fig. 4D presents 2D latent response maps depicting the evolution of microstructural geometry as two latent dimensions vary simultaneously.

The coefficients in the phenomenological formula quantify the influence of the geometric features on specific material properties. According to the value of the coefficients (fully detailed in the Supplementary Materials), the features extracted from c_1 are primarily related to the maximum modulus of elasticity, while c_2 predominantly affects the relative surface area. The directional features extracted by c_3 determine the principal directions of the elasticity tensor.

The generated materials with extrapolated latent codes are demonstrated in the second row of each subfigure in Fig. 4. When keeping the other two latent codes fixed, expanding c_1 leads to a substantial exploration of the range of the maximum elastic modulus, while expanding c_2 primarily explores the range of the contour length. Our exploration method performs well even with angularly periodic geometric features. Although our training dataset only covers a 120° range of variation, we can complement the remaining 60°. By using the periodic nature of angles, we can generate continuous angle information for any value of latent code. The generated results for varying latent codes are shown in movie S1. Consequently, as shown in Fig. 5A, the latent code space is mapped to the property space. The gamut of properties exhibited by the generated materials not only nearly covers that of the dataset but also obviously expands the property space. This enables us to design materials with characteristics beyond those in the dataset and explore a broader material space.

To further validate the design capabilities of GNDM, we fabricate selected materials with designed microstructures via 3D printing, and then measure experimentally the Young's moduli and the principal orientations of the printed samples (fig. S3). Details of the fabrication and measurement procedures are provided in the Supplementary Materials. We also conduct direct FE simulations over the same samples. We selected 10 geometric parameter sets within the expanded parameter range, aiming to cover the broadened spectrum of material properties in our design space. Five microstructure realizations were generated for each parameter set to account for the stochastic variability in the design process. For each microstructure, mechanical tests were conducted in both the transverse and longitudinal directions, with three identical specimens printed and tested for each direction. Comprehensive descriptions of the experimental procedures and experiment results data are provided in table S1. The markers in Fig. 5B refer to the target material properties and the corresponding properties measured through experiments and FEM. The color of the central points of each marker represents the value of relative surface area. Despite the inherent randomness in the microstructures, materials generated using the same set of parameters exhibit similar material properties that closely align with the expected properties. This implies that the material properties are indeed associated with hidden invariant geometric features of the disordered microstructures, which have been successfully found by the GNDM. In Fig. 5 (C and D), we present the comparison between experimental measurements and target properties. The measurements closely follow the targets, with R^2(coefficient of determination) = 0.897 for normalized stiffness E/E_{hard} and $R^2 = 0.963$ for rotation θ. The larger scatter observed in E/E_{hard} indicates that stiffness is more sensitive than rotation to fabrication imperfections, boundary condition mismatches during testing, and intrinsic material variability, whereas θ is reproduced robustly across specimens. In addition, fig. S4 provides a detailed comparison of FEM predictions with both the target and experimental data. FEM predictions closely reproduce the targets for both metrics, indicating that the observed discrepancies between experimental measurements and target values stem from two sources: the stochastic variability inherent in the material design and errors introduced during the experimental process. Since the relative surface area is not easily measurable in experiments, we directly compute it using the algorithm to calculate these results. The simulations follow the targets with moderate fidelity, yielding $R^2 = 0.744$. While a small number of experimental groups exhibit larger deviations from the target values, which reduces the overall accuracy, the majority of the data show good agreement with the designed targets.

To evaluate the distribution of designed materials corresponding to the 10 selected parameter sets and the influence of sample size on material properties, we generated 500 realizations for each set and computed their effective properties using numerical simulations (see figs. S6 and S7). It is worth noting that since our model learns the distribution information of geometric features, the influence of randomness on material properties tends to decrease as the sample size increases. To test this assertion, we numerically computed results for microstructural samples of increasing size: 64 × 64, 128 × 128, and 256 × 256. Figure S5C presents the deviations from the target properties for each parameter set across the three resolutions, along with the standard deviation shown as error bars. It is evident that as the microstructure size increases, the SD decreases, indicating that the extracted geometric parameters reliably capture the statistical distribution of the material features. Although the specific microstructure realizations are stochastic, the overall material properties converge toward the predicted values as the system size increases, and the fluctuations become smaller.

For instance, we demonstrate how a disordered microstructure can exhibit different material properties in distinct regions. This capability is highlighted by designing a "cat" structure that deforms when compressed at various points, such as the "tail," "legs," and "head" (Fig. 5, E and F). Specifically, the cat's head was designed to be relatively soft, while the back was made stiff. The belly and legs were constructed using a functionally graded material that gradually

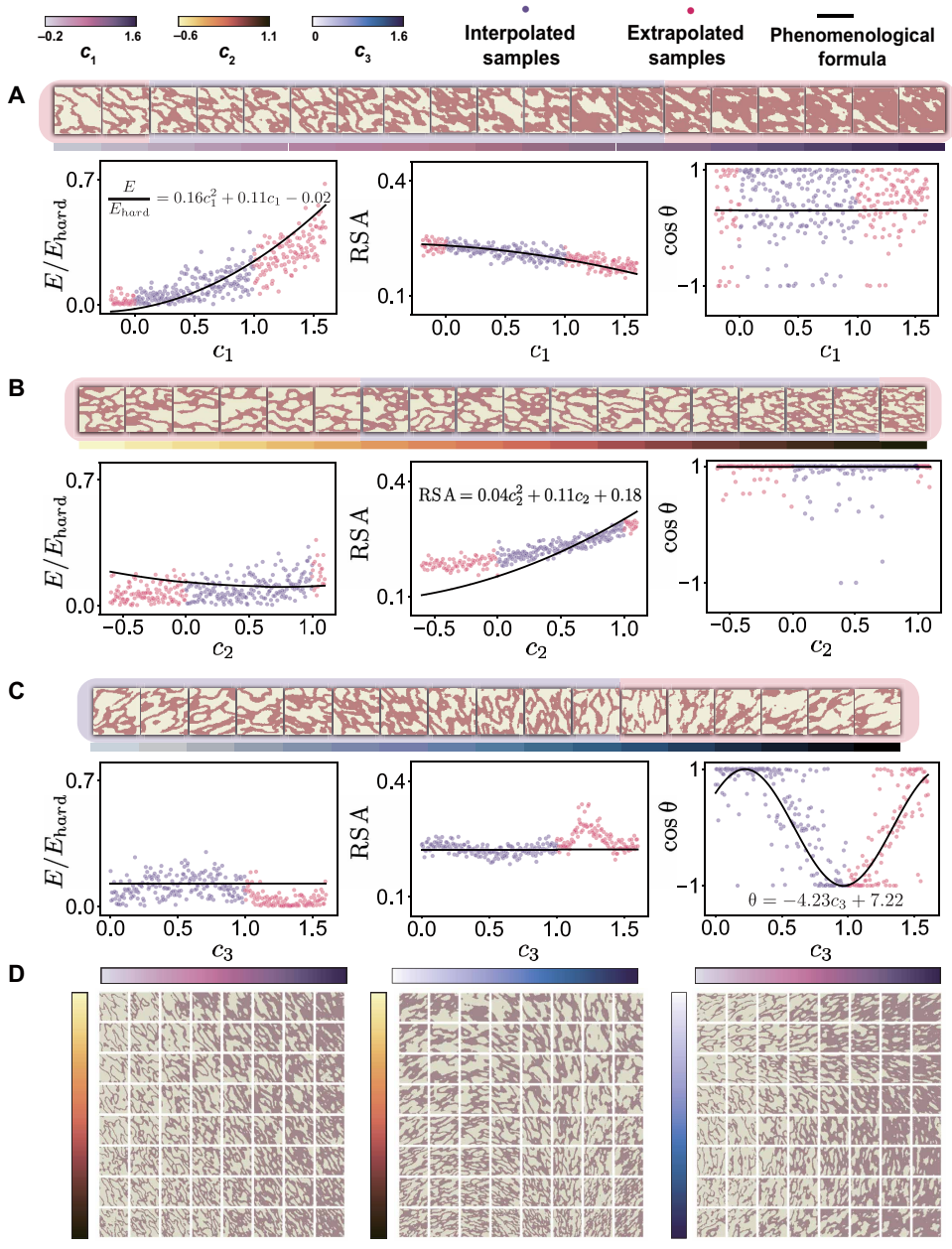

Fig. 4. Geometric feature extraction and inverse design considering three different material properties concurrently. The samples are generated with gradually changing interpolated and extrapolated latent codes. The maximum Young's modulus (normalized by E_{hard}, the Young's modulus of the hard material), RSA (the relative surface area), and θ (the orientation of the maximum modulus) of these samples are calculated by the physical module and predicted by the phenomenological formula. (**A**) Results for varying c_1 and fixed $c_2 = 0.47$ and $c_3 = 0.52$. (**B**) Results for varying c_2 and fixed $c_1 = 0.63$ and $c_3 = 0.19$. (**C**) Results for varying c_3 and fixed $c_1 = 0.69$ and $c_2 = 0.56$. (**D**) Latent-space atlas of generated microstructures. Representative microstructures sampled by sweeping pairs of latent coordinates (c_1, c_2, c_3). Each grid shows a 2D slice through the 3D latent space with the remaining coordinate held fixed at its median value: left, $c_1 - c_2$; middle, $c_2 - c_3$; right, $c_1 - c_3$. Color bars indicate the value ranges of each coordinate.

increases in stiffness from bottom to top. In addition, the tail was designed as an anisotropic material, aligned along its length.

To enable a broader range of applications, we extend GNDM to comprehend and design 3D disordered metamaterials. This can be done by replacing the 2D CNN with a 3D CNN for all four neural network modules, i.e., the generator, discriminator, feature extractor, and observer. The physical simulation tools must be adapted for 3D systems. Similar to the 2D case with a single pair of material property and geometric feature, we also use a single latent code to characterize the relationship of the pair. The results are shown in Fig. 3 (D and E). Here, we set Young's modulus as the primary property of interest. Consistent with the observations from the 2D case, we found that Young's modulus is strongly correlated with the relative proportions of the two constituent materials. This example demonstrates that our model can be effectively applied to a broader range of real-world scenarios.

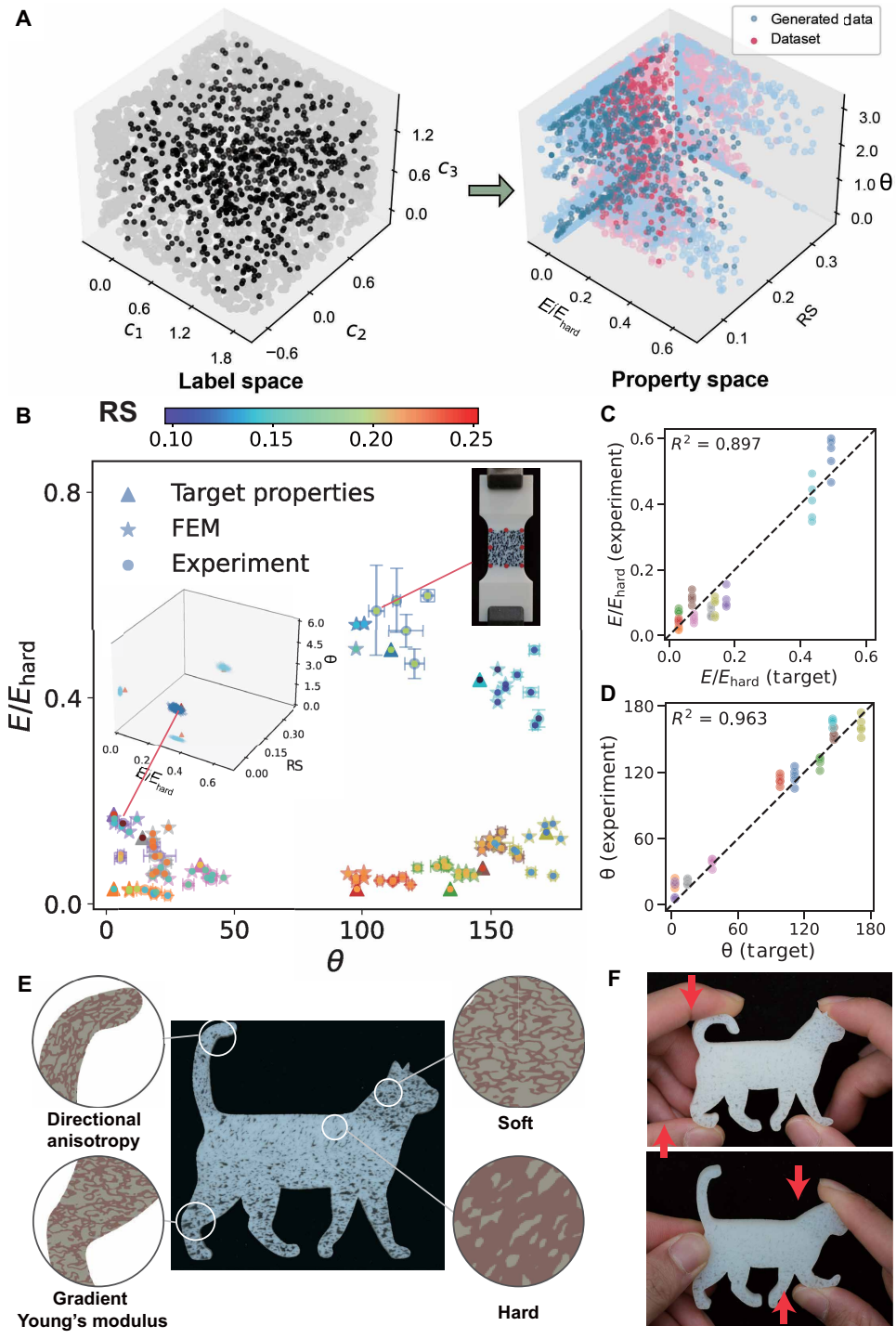

Fig. 5. Experimental validation of disordered materials generated by GNDM. (**A**) Mapping from the geometric feature parameter space to the property space. A comparison of the coverage range of properties between the generated materials and the materials in the initial dataset within the property space. (**B**) Results showing the coverage of properties by different parameter sets. Each point cloud in a given color corresponds to a specific parameter set. Scatter plots show sample properties calculated by the simulation tools and those measured by experiments. The color of the center indicates the relative surface area. (**C** and **D**) Relative maximum Young's modulus and anisotropic direction θ of target properties versus experiment validation. Cat deformation under compression, owing to its heterogeneous microstructures. (**E**) 3D printed structure before compression. The zoomed-in views show the different regions with different functions. (**F**) Structure during compression. The arrows show the direction of loading. R^2, coefficient of determination.

DISCUSSION

The results presented in this study demonstrate the remarkable capability of the GNDM in understanding the intricate property-structure relationship of disordered metamaterials. Leveraging the concept of self-supervised learning together with necessary, minimal predefined processing and physics-informed priors, our model effectively captures the geometric features of disordered microstructures, extracts their distribution parameters (i.e., the invariance), and establishes phenomenological formulae to relate them to the distribution parameters of material properties. To reduce the dimension of the design space of disordered metamaterials, conventional approaches impose artificial geometric restrictions, such as periodicity or symmetry. However, our model achieves the desired properties without any restriction on the material microstructures, thanks to the power of artificial intelligence. Nevertheless, the autonomy of GNDM lies in its ability to automatically find geometric descriptors that are not manually annotated and to uncover quantitative structure-property relationships through phenomenological formulae. The interpretability of the latent space primarily results from unsupervised extraction via mutual-information maximization. Hierarchical injection was adopted to better disentangle geometric features across different scales, and this strategy is generally applicable to different material systems and network architectures. While certain inductive elements, such as periodic encodings, were introduced to capture orientation-related features, they serve as practical adjustments to the inherent limitations of CNN architectures rather than as methodological constraints of the framework. In the future, we will devote ourselves to explore other types of AI architectures, like graph neural networks that can have better performance on aspects such as rotational invariance to further minimize the level of human engineering and preprocessing, so that a higher level of autonomy can be achieved. The proposed model holds substantial promise for two crucial applications. First, it enables us to gain insights into the intricate relationship between the geometric features and their resulting properties. By comprehending these relationships, it enhances our understanding of the material behavior of nonperiodic, disordered metamaterials. Second, the discovered relationship between the probability distributions of the geometric features and the material properties opens up previously unidentified avenues for the design of disordered microstructures toward desired material properties using sampling.

First, we emphasize that GNDM is, in principle, applicable to a broad class of disordered materials. This generality stems from the fact that our approach processes the geometry directly from images using neural networks, without imposing any artificial geometric constraints such as periodicity or symmetry. To verify this, we conducted additional tests on circular inclusion-type microstructures (fig. S11). GNDM successfully learned to capture the inclusion fraction and correlated it with the effective stiffness. Moreover, GNDM is not limited to only two materials; it can be generalized to handle multiphase disordered materials. To generalize to a K-phase system, we modify the final layer to output a K-dimensional vector per pixel, $\mathbf{z} = (z_1, z_2, \ldots, z_K)$, which is transformed via a softmax function into a valid probability distribution over the K phases. The predicted material phase at each pixel is then assigned to the phase with the highest probability, and the standard cross-entropy loss is used during training. Only the material input and the simulation tools need to be adjusted for the multiphase setting, while the remaining components of the GNDM framework remain unchanged. In the future, GNDM could be applied to complex biological materials, such as wood and bone, concerning multiphysics responses. It is also possible to incorporate state-of-the-art neural network architectures and simulation tools. In addition, the phenomenological formula, which in this work is represented as polynomials, can be expanded to more complex forms, thus extending its applicability to multiple physical properties, such as fracture resistance, negative refraction, thermal conductivity, etc.

MATERIALS AND METHODS

Dataset

The dataset consists of 1000 2D disordered microstructural images for the single-parameter case and 1500 images for the three-parameter case. A set of GRFs are used to mathematically characterize the spatial patterns of these materials. Specifically, for a 2D domain $D \subset \mathbb{R}^2$, we prescribe a (real-valued) random field for each point in that domain, i.e., $\{Z(\mathbf{x}): \mathbf{x} \in D\}$. The value of this field can be described by the following vector of random variables $\mathbf{Z} = \left[Z(\mathbf{x}_1), Z(\mathbf{x}_2), \ldots, Z(\mathbf{x}_N)\right]^T$, where $\mathbf{x}_1, \ldots, \mathbf{x}_N \in D$.

For each $\mathbf{x} \in D$, $Z(\mathbf{x})$ is a random variable. We define the mean function $\mu(\mathbf{x}) = \mathbb{E}[Z(\mathbf{x})]$ and the covariance function

$$C(\mathbf{x}, \mathbf{y}) = \mathrm{Cov}\left[Z(\mathbf{x}), Z(\mathbf{y})\right] = \mathbb{E}\left\{\left[Z(\mathbf{x}) - \mu(\mathbf{x})\right]\left[Z(\mathbf{y}) - \mu(\mathbf{y})\right]\right\}, \mathbf{x}, \mathbf{y} \in D \quad (1)$$

Suppose $D = [0, 1] \times [0, 1]$ and divide D into $n_1 \times n_2$ rectangular elements. Select $N = n_1 \times n_2$ sample points by taking the mid-points of the rectangular elements and arranging them in lexicographical order. A GRF is a second-order field, such that the vector of random variables follows the multivariate Gaussian distribution for any $\mathbf{x}_1, \ldots, \mathbf{x}_N \in D$. For single-parameter isotropic GRF, the vector $\mathbf{Z}$ follows a normal distribution and $N(\mu, C)$ the covariance function $C(\mathbf{x}, \mathbf{y})$ is chosen so that

$$C(\mathbf{x}, \mathbf{y}) = \int_{\mathbb{R}^2} e^{-2\pi i \ \mathbf{p}\cdot(\mathbf{x}-\mathbf{y})} \gamma(\mathbf{p}) d\mathbf{p} \quad (2)$$

with

$$\gamma(\mathbf{p}) = \left(m + \frac{p_1^{2k} + p_2^{2k}}{l}\right)^{-n} \quad (3)$$

where $k, n \in \mathbb{N}, m, l \in \mathbb{R}_+$, and $\mathbf{p} = (p_1, p_2) \in \mathbb{R}^2$. Here, we take the value for $k = 1, n = 2$, $m = 10^{-3}$, and $l = 10^4$. The final images for the single parameter are constructed by performing a lever cut through $\mathbf{Z}$ at a threshold value z_1. Such a cut delineates an interface that defines the hard phase and soft phase. The hard phase is defined by the region where $Z < z_1$, while the soft phase is defined by the region where $Z > z_1$.

In the case of a three-parameter GRF, anisotropy is introduced by assigning distinct scales to different directions in the covariance function. This is achieved by redefining the function $\gamma(\mathbf{p})$ as

$$\gamma(\mathbf{p}) = \left[m + \frac{\left(p_1\cos\theta + p_2\sin\theta\right)^2}{l_1} + \frac{\left(-p_1\sin\theta + p_2\cos\theta\right)^2}{l_2}\right]^{-2} \quad (4)$$

where θ represents the orientation of anisotropy and l_1, l_2 are the scale factors in the principal orientations. To enhance the continuity of the hard phase, the final images for three-parameter cases are generated by implementing two-level cuts through $\mathbf{Z}$ at threshold

values z_1 and z_2, where $z_1 < z_2$. The hard phase is defined within the region where $z_1 < \mathbf{Z} < z_2$, while the remaining region represents the soft phase.

Loss for GNDM

The generator and the discriminator adopt the same losses as defined in the WGAN-GP (*40*), with their architectures detailed in the Supplementary Materials. We need to determine the dimensionality of the latent code in advance. The feature extractor, inspired by the DCGAN discriminator, encompasses a latent code output mechanism shown in Fig. 2, whose output dimension matches the predefined latent code dimension. The observer net is built upon the ResNet architecture, and the number of output variables is contingent on the properties under consideration.

To tackle the training difficulties associated with GANs, we adopt the WGAN-GP (*40*) approach. We optimize the generator and discriminator networks using the objective function $W(\mathbb{P}_r, \mathbb{P}_g)$ with a gradient penalty. Here, $W(\mathbb{P}_r, \mathbb{P}_g)$ is an efficient approximation of the Wasserstein distance, which quantifies the proximity between the generator's distribution and the data distribution (*40*). The gradient penalty is integrated into the discriminator to enforce the Lipschitz constraint, thereby bolstering the stability and convergence of the training process. The generator loss function is defined as

$$L_G = -\mathbb{E}_{z\sim p(z),c\sim p(c)}\{D[G(z,c)]\} \tag{5}$$

The discriminator loss function is defined as

$$L_D = \mathbb{E}_{z\sim p(z),c\sim p(c)}\{D[G(z,c)]\} - \mathbb{E}_{x\sim \mathbb{P}_r}[D(x)] + \lambda_1 \mathbb{E}_{\hat{x}\sim \mathbb{P}_{\hat{x}}}\left[\|\nabla_{\hat{x}} D(\hat{x})\|_p - 1\right]^2 \tag{6}$$

where G is defined as the generator, D is defined as the discriminator, and Q is defined as the feature extractor; x can be viewed as $x \sim \mathbb{P}_r$; $\mathbb{P}_{\hat{x}}$ is defined as sampling uniformly along straight lines between pairs of points sampled from the data distribution $\mathbb{P}_r$ and the generator distribution $\mathbb{P}_g$.

To automatically extract the probability distribution of geometric feature parameters of materials, we draw inspiration from InfoGAN (*41*). We integrate a lower bound on mutual information into our model to facilitate the learning of geometrically interpretable and disentangled features of the materials. The mutual information $I[c; G(z,c)]$ is maximized by maximizing the lower bound $L_I(G,Q)$, given by

$$L_I(G,Q) = \mathbb{E}_{z\sim p(z),c\sim p(c)}\left\{\log Q[c|G(z,c)]\right\} + H(c) \tag{7}$$

Here, $H(c)$ represents the entropy of c.

The observer is optimized using real physical data from both the dataset samples and the generated samples with MSE loss

$$L_O = \|O[G(z,c)] - S[G(z,c)]\| + \|O(x) - S(x)\| \tag{8}$$

Here, O represents the observer, and S corresponds to the simulation tools. Furthermore, in the process of optimizing the coefficients of the phenomenological formula and the generator, the objective is to minimize the following MSE loss L_F

$$L_F = \|O[G(z,c)] - F(c)\| \tag{9}$$

where F represents the phenomenological formula.

Calculation of material properties

The effective Young's modulus of the materials was calculated using the FEM based on asymptotic homogenization. For the FEM calculation, we first converted image pixels into a corresponding mesh structure using linear quadrilateral elements. We only consider the elastic behavior of the microstructures here. Based on asymptotic homogenization, the macroscopic behavior of the heterogeneous material can be determined by solving a corresponding cell problem (see the Supplementary Materials for details), assuming an infinite tiling of identical structures with periodic boundary conditions. The cell problem is then solved by FEM by converting the corresponding governing equation into the form of $\mathrm{Ku} = f$. Once the effective elastic tensor is determined, the orientation of the principal tensile modulus was obtained by rotating the coordinate system, and the orientation of the principal modulus was calculated. See the Supplementary Material for details. The relative surface area is computed using the OpenCV library.

Supplementary Materials

The PDF file includes:

Supplementary Text
Table S1
Figs. S1 to S11
Legends for movies S1 and S2
References

Other Supplementary Material for this manuscript includes the following:

Movies S1 and S2

REFERENCES

1. L. J. Gibson, The hierarchical structure and mechanics of plant materials. *J. R. Soc. Interface* **9**, 2749–2766 (2012).
2. J. Aizenberg, J. C. Weaver, M. S. Thanawala, V. C. Sundar, D. E. Morse, P. Fratzl, Skeleton of Euplectella sp.: Structural hierarchy from the nanoscale to the macroscale. *Science* **309**, 275–278 (2005).
3. S. Krauss, E. Monsonego-Ornan, E. Zelzer, P. Fratzl, R. Shahar, Mechanical function of a complex three-dimensional suture joining the bony elements in the shell of the red-eared slider turtle. *Adv. Mater.* **21**, 407–412 (2009).
4. C. Perrin, Compositional heterogeneity and microstructural diversity of coral skeletons: Implications for taxonomy and control on early diagenesis. *Coral Reefs* **22**, 109–120 (2003).
5. A. Torres, A. A. Trikanad, C. A. Aubin, F. M. Lambers, M. Luna, C. M. Rimnac, P. Zavattieri, C. J. Hernandez, Bone-inspired microarchitectures achieve enhanced fatigue life. *Proc. Natl. Acad. Sci. U.S.A.* **116**, 24457–24462 (2019).
6. M. Zaiser, S. Zapperi, Disordered mechanical metamaterials. *Nat. Rev.* **5**, 679–688 (2023).
7. H. Rhee, M. Horstemeyer, Y. Hwang, H.-S. Lim, H. Kadiri, W. Trim, A study on the structure and mechanical behavior of the *terrapene carolina* carapace: A pathway to design bio-inspired synthetic composites. *Mater. Sci. Eng. C* **29**, 2333–2339 (2009).
8. J. T. Overvelde, K. Bertoldi, Relating pore shape to the non-linear response of periodic elastomeric structures. *J. Mech. Phys. Solids* **64**, 351–366 (2014).
9. C. M. Portela, A. Vidyasagar, S. Krödel, T. Weissenbach, D. W. Yee, J. R. Greer, D. M. Kochmann, Extreme mechanical resilience of self-assembled nanolabyrinthine materials. *Proc. Natl. Acad. Sci. U.S.A.* **117**, 5686–5693 (2020).
10. P. Wang, F. Yang, B. Zheng, P. Li, R. Wang, Y. Li, H. Fan, X. Li, Breaking the tradeoffs between different mechanical properties in bioinspired hierarchical lattice metamaterials. *Adv. Funct. Mater.* **33**, 2305978 (2023).
11. F. Wang, M. Brøns, O. Sigmund, Non-hierarchical architected materials with extreme stiffness and strength. *Adv. Funct. Mater.* **33**, 2211561 (2023).
12. D. Schurig, J. J. Mock, B. J. Justice, S. A. Cummer, J. B. Pendry, A. F. Starr, D. R. Smith, Metamaterial electromagnetic cloak at microwave frequencies. *Science* **314**, 977–980 (2006).
13. F. Magnus, B. Wood, J. Moore, K. Morrison, G. Perkins, J. Fyson, M. C. K. Wiltshire, D. Caplin, L. F. Cohen, J. B. Pendry, A d.c. magnetic metamaterial. *Nat. Mater.* **7**, 295–297 (2008).
14. J. Li, L. Fok, X. Yin, G. Bartal, X. Zhang, Experimental demonstration of an acoustic magnifying hyperlens. *Nat. Mater.* **8**, 931–934 (2009).
15. N. Fang, D. Xi, J. Xu, M. Ambati, W. Srituravanich, C. Sun, X. Zhang, Ultrasonic metamaterials with negative modulus. *Nat. Mater.* **5**, 452–456 (2006).

16. T. A. Schaedler, A. J. Jacobsen, A. Torrents, A. E. Sorensen, J. Lian, J. R. Greer, L. Valdevit, W. B. Carter, Ultralight metallic microlattices. *Science* **334**, 962–965 (2011).
17. J. I. Lipton, R. MacCurdy, Z. Manchester, L. Chin, D. Cellucci, D. Rus, Handedness in shearing auxetics creates rigid and compliant structures. *Science* **360**, 632–635 (2018).
18. C. Luo, Y. Song, C. Zhao, S. Thirumalai, I. Ladner, M. A. Cullinan, J. B. Hopkins, Design and fabrication of a three-dimensional meso-sized robotic metamaterial with actively controlled properties. *Mater. Horiz.* **7**, 229–235 (2020).
19. M. J. Silva, L. J. Gibson, The effects of non-periodic microstructure and defects on the compressive strength of two-dimensional cellular solids. *Int. J. Mech. Sci.* **39**, 549–563 (1997).
20. R. A. Metzler, F. Barthelat, J. J. Wilker, Disordered structures in biology can provide material properties not obtained with precise hierarchy. *Adv. Funct. Mater.* **29**, 1805734 (2019).
21. D. Rayneau-Kirkhope, S. Bonfanti, S. Zapperi, Density scaling in the mechanics of a disordered mechanical meta-material. *Appl. Phys. Lett.* **114**, 111902 (2019).
22. Y. Jia, K. Liu, X. S. Zhang, Modulate stress distribution with bio-inspired irregular architected materials towards optimal tissue support. *Nat. Commun.* **15**, 4072 (2024).
23. D. R. Reid, N. Pashine, J. M. Wozniak, H. M. Jaeger, A. J. Liu, S. R. Nagel, J. J. de Pablo, Auxetic metamaterials from disordered networks. *Proc. Natl. Acad. Sci. U.S.A.* **115**, E1384–E1390 (2018).
24. Y. Liu, B. Xia, K. Liu, Y. Zhou, K. Wei, Robustness and diversity of disordered structures on sound absorption and deformation resistance. *J. Mech. Phys. Solids* **190**, 105751 (2024).
25. K. Liu, R. Sun, C. Daraio, Growth rules for irregular architected materials with programmable properties. *Science* **377**, 975–981 (2022).
26. M. A. Bessa, R. Bostanabad, Z. Liu, A. Hu, D. W. Apley, C. Brinson, W. Chen, W. K. Liu, A framework for data-driven analysis of materials under uncertainty: Countering the curse of dimensionality. *Comput. Method Appl. Mech. Eng.* **320**, 633–667 (2017).
27. S. Torquato, H. Haslach Jr., Random heterogeneous materials: Microstructure and macroscopic properties. *Appl. Mech. Rev.* **55**, B62–B63 (2002).
28. A. J. Lew, K. Jin, M. J. Buehler, Designing architected materials for mechanical compression via simulation, deep learning, and experimentation. *NPJ Comput. Mater.* **9**, 80 (2023).
29. D. Lee, W. W. Chen, L. Wang, Y. C. Chan, W. Chen, Data-driven design for metamaterials and multiscale systems: A review. *Adv. Mater.* **36**, e2305254 (2024).
30. R. Kulagin, Y. Beygelzimer, Y. Estrin, A. Schumilin, P. Gumbsch, Architectured lattice materials with tunable anisotropy: Design and analysis of the material property space with the aid of machine learning. *Adv. Eng. Mater.* **22**, 2001069 (2020).
31. R. Van Mastrigt, M. Dijkstra, M. van Hecke, C. Coulais, Machine learning of implicit combinatorial rules in mechanical metamaterials. *Phys. Rev. Lett.* **129**, 198003 (2022).
32. B. Peng, Y. Wei, Y. Qin, J. Dai, Y. Li, A. Liu, Y. Tian, L. Han, Y. Zheng, P. Wen, Machine learning-enabled constrained multi-objective design of architected materials. *Nat. Commun.* **14**, 6630 (2023).
33. Z. Yu, P. Thakolkaran, K. Shea, T. Stanković, Artificial neural network supported design of a lattice-based artificial spinal disc for restoring patient-specific anisotropic behaviors. *Comput. Biol. Med.* **152**, 106475 (2023).
34. S. Kumar, S. Tan, L. Zheng, D. M. Kochmann, Inverse-designed spinodoid metamaterials. *NPJ Comput. Mater.* **6**, 73 (2020).
35. F. V. Senhora, E. D. Sanders, G. H. Paulino, Optimally-tailored spinodal architected materials for multiscale design and manufacturing. *Adv. Mater.* **34**, e2109304 (2022).
36. B. Li, C. Huang, X. Li, S. Zheng, J. Hong, Non-iterative structural topology optimization using deep learning. *Comput. Aided Des.* **115**, 172–180 (2019).
37. A. H. Nobari, W. Chen, F. Ahmed, Range-constrained generative adversarial network: Design synthesis under constraints using conditional generative adversarial networks. *J. Mech. Des.* **144**, 021708 (2022).
38. S. Noguchi, J. Inoue, Stochastic characterization and reconstruction of material microstructures for establishment of process-structure-property linkage using the deep generative model. *Phys. Rev. E* **104**, 025302 (2021).
39. I. Goodfellow, J. Pouget-Abadie, M. Mirza, B. Xu, D. Warde-Farley, S. Ozair, A. Courville, Y. Bengio, Generative adversarial networks. *Commun. ACM* **63**, 139–144 (2020).
40. I. Gulrajani, F. Ahmed, M. Arjovsky, V. Dumoulin, A. Courville, Improved training of wasserstein gans. *Adv. Neural Inf. Process Syst.* **30**, 5769–5779 (2017).
41. X. Chen, A. Karbasi, F. W. Crawford, Estimating the size of a large network and its communities from a random sample. *Adv. Neural Inf. Process Syst.* **29**, 3072–3080 (2016).
42. B. Zhu, M. Skouras, D. Chen, W. Matusik, Two-scale topology optimization with microstructures. *ACM Trans. Graph.* **36**, 1 (2017).
43. L. Makatura, B. Wang, Y. L. Chen, B. Deng, C. Wojtan, B. Bickel, W. Matusik, Procedural metamaterials: A unified procedural graph for metamaterial design. *ACM Trans. Graph.* **42**, 1–19 (2023).
44. H. Li, Z. Luo, L. Gao, Q. Qin, Topology optimization for concurrent design of structures with multi-patch microstructures by level sets. *Comput. Methods Appl. Mech. Eng.* **331**, 536–561 (2018).
45. M. Xiao, X. Liu, Y. Zhang, L. Gao, J. Gao, S. Chu, Design of graded lattice sandwich structures by multiscale topology optimization. *Comput. Methods Appl. Mech. Eng.* **384**, 113949 (2021).
46. G. Bertolino, M. Montemurro, Two-scale topology optimisation of cellular materials under mixed boundary conditions. *Int. J. Mech. Sci.* **216**, 106961 (2022).
47. F. Liu, Z. Mao, P. Zhang, D. Z. Zhang, J. Jiang, Z. Ma, Functionally graded porous scaffolds in multiple patterns: New design method, physical and mechanical properties. *Mater. Des.* **160**, 849–860 (2018).
48. M. F. Ashby, L. J. Gibson, Cellular solids: Structure and properties (Cambridge Univ. Press, 1997), pp. 175–231.
49. K. Sano, Y. Ishida, T. Aida, Synthesis of anisotropic hydrogels and their applications. *Angew. Chem. Int. Ed.* **57**, 2532–2543 (2018).
50. A. Radford, L. Metz, S. Chintala, Unsupervised representation learning with deep convolutional generative adversarial networks. arXiv:1511.06434 [cs.LG] (2015).
51. T. Salimans, W. Zaremba, V. Cheung, X. Chen, I. Goodfellow, A. Radford, Improved techniques for training gans. *Adv. Neural Inf. Process. Syst.* **29**, 6597–6607 (2016).
52. H. De Vries, F. Strub, J. Mary, H. Larochelle, O. Pietquin, A. Courville, Modulating early visual processing by language. *Adv. Neural Inf. Process. Syst.* **30**, (2017).
53. G. Bradski, The opencv library. *Dr. Dobb's Journal: Software Tools for the Professional Programmer* **25**, 120–123 (2000).
54. J. Fish, *Practical Multiscaling* (John Wiley & Sons, 2013).

Acknowledgment
Funding: C.D. acknowledges the support from the Gary Clinard Innovation Fund. **Author contributions:** Conceptualization: K.L. and S.M. Methodology: K.L., S.M., M.S., and C.D. Investigation: M.S. Visualization: M.S. Supervision: K.L., S.M. and CD. Resources: S.M. Validation: K.L., S.M., M.S. Formal analysis: M.S. Software: M.S. and S.M. Writing—original draft: M.S. Writing—review and editing: K.L., S.M., and C.D. **Competing interests:** The authors declare that they have no competing interests. **Data and materials availability:** All data and code needed to evaluate and reproduce the results in the paper are present in the paper and/or the Supplementary Materials.

Submitted 26 March 2025
Accepted 1 December 2025
Published 2 January 2026
10.1126/sciadv.adx7389